



## Article

# A New Upwelling Index for the Moroccan Atlantic Coast for the Period between 1982–2021

Hanae Belmajdoub <sup>1,\*</sup>, Khalid Minaoui <sup>1</sup>, Anass El Aouni <sup>2</sup>, Karim Hilmi <sup>3</sup>, Rachid Saadane <sup>4</sup> and Abdellah Chehri <sup>5</sup>

<sup>1</sup> LRIT Laboratory, Faculty of Sciences, Mohammed V University in Rabat, Rabat B.P.1014, Morocco

<sup>2</sup> Institut des Géosciences de l'Environnement, Université Grenoble Alpes, CNRS, IRD, Grenoble-INP, Saint-Martin-d'Hères, 38400 Grenoble, France

<sup>3</sup> Institut National de Recherche Halieutique, 02 Bd Sidi Abderrahmane, Ain Diab, Casablanca 20100, Morocco

<sup>4</sup> SIRC-LaGeS, Hassania School of Public Works, Casablanca 20000, Morocco

<sup>5</sup> Department of Mathematics and Computer Science, Royal Military College of Canada, Kingston, ON K7K 7B4, Canada; chehri@rmc.ca

\* Correspondence: hanae\_belmajdoub@um5.ac.ma

**Abstract:** Being a component of the Eastern Boundary Upwelling (EBU) ecosystem, Morocco's Atlantic coast presents high biological production throughout the year, with seasonal variations in upwelling dynamics. This characterization reflects the inherent nature of EBU's ecosystems. In this work, we develop a novel methodology to compute a new upwelling index based on the analysis of sea surface temperature (SST) images. Our new upwelling index is not only simple to calculate but also efficient. Indeed, it is limited only to the upwelling region, which has allowed the improvement of the quantification and analysis of the seasonal and interannual variability of the upwelling dynamics. The new proposed upwelling index is based on the application of a recent segmentation method that allows for the monitoring of upwelling dynamics using satellite observations. The proposed upwelling index is applied to a 40-year database of weekly SST images covering the period from 1982 to 2021, and the results are used to analyze seasonal and interannual variations of the upwelling in the region.

**Keywords:** sea surface temperature; wind; Moroccan coastal upwelling; new upwelling index; anomalies



**Citation:** Belmajdoub, H.; Minaoui, K.; El Aouni, A.; Hilmi, K.; Saadane, R.; Chehri, A. A New Upwelling Index for the Moroccan Atlantic Coast for the Period between 1982–2021. *Remote Sens.* **2023**, *15*, 3459. <https://doi.org/10.3390/rs15143459>

Academic Editors: Jian Sun, Weizeng Shao, Changlong Guan and Alexander Babanin

Received: 7 June 2023

Revised: 2 July 2023

Accepted: 7 July 2023

Published: 8 July 2023



**Copyright:** © 2023 by the authors. Licensee MDPI, Basel, Switzerland. This article is an open access article distributed under the terms and conditions of the Creative Commons Attribution (CC BY) license (<https://creativecommons.org/licenses/by/4.0/>).

## 1. Introduction

The Canary Current System is recognized as one of the four major eastern boundary currents worldwide, which are strongly influenced by the upwelling phenomenon [1]. The Moroccan Atlantic coast, situated within the central region of the Canary Current System, experiences a distinct and dominant upwelling pattern that persists throughout the year [2]. This region is characterized by persistent upwelling activity, with spatial variability throughout the year [3]. Upwelling is a phenomenon defined by the rise of deep ocean water to the surface, resulting in the emergence of cold waters enriched with essential nutrients such as nitrogen and phosphorus [4]. These nutrient-rich waters facilitate the growth of phytoplankton and the formation of cyanobacterial blooms, which serve as the primary food source for fish and other marine species [5].

The upwelling along the Atlantic coast of Morocco is primarily driven by strong equatorward trade winds. These trade winds blow across the sea surface, causing surface water to be displaced offshore and enabling the upwelling of cold, nutrient-rich water from the depths [6]. This process sustains high levels of productivity in the marine ecosystems along Africa's west coast, where upwelling is particularly intense. The wind regime in this region, influenced by the seasonal migration of the intertropical convergence zone and the Azores high-pressure cell, plays a critical role in generating quasi-permanent Ekman pumping

and coastal upwelling in the Canary Upwelling ecosystem, a typical Eastern Boundary Upwelling System [7]. The northwest African upwelling area experiences particularly vigorous equatorward trade winds that significantly influence the strength and duration of the upwelling phenomenon. These winds create a divergence of surface waters, allowing colder water from the deep to ascend to the surface. As a result, distinct physical and chemical properties are observed, along with higher nutrient concentrations [8]. Equatorward trade winds, driven by the seasonal migration of the intertropical convergence zone and the Azores high-pressure cell, are the primary driver of upwelling in this region, contributing to nutrient enrichment and the productivity of marine ecosystems [9,10].

Detecting upwellings is of great interest to oceanographers due to their implications for studying various physical processes in the ocean. Strong upwelling, for instance, can lead to phytoplankton blooms, which are essential for maintaining a healthy marine ecosystem [11]. Upwelling also transports nutrient-rich water from the depths to the surface, providing favorable conditions for fisheries. Understanding the physical mechanisms behind upwelling has revealed a series of processes that contribute to this phenomenon. These include variations in sea surface temperature (SST), wind-driven current velocities, and water density differences.

Wind patterns are used to quantify the intensity of upwelling. Traditional approaches involve computing the Coriolis forces responsible for Cross-Shore Ekman Transport (CSET) based on wind data [12]. However, these traditional methods often overlook the influence of the continental shelf's bathymetry, limiting their ability to represent the complex two-dimensional spatial organization of upwelling, such as coastal upwelling cells, cape effects, and filaments.

In addition to wind patterns, sea surface temperature (SST) and nutrient-rich water in coastal areas serve as important indicators for determining the intensity of upwelling. SST images provide an overview of the surface ocean skin temperature distribution within the top few micrometers of the surface layer [13].

For example, authors in [8,12,14–16] used the remote sensing data of SST to calculate the upwelling index to characterize the main patterns of seasonal and interannual upwelling variation. For instance, this index is computed as a simple thermal difference between warmer offshore waters and cold coastal waters at the same latitude over the northwest African upwelling area.

Several works have objectively relied on automatic tools to extract and identify upwelling to improve the calculation of the above-mentioned index. The authors in [17] were focused on the southern part of the Atlantic coast of Morocco for the automatic detection of upwelling. They used Fuzzy c-means (FCM) and region-growing algorithms to detect and extract the phenomenon and then computed the upwelling index. On the other hand, authors in [2,3,18] proposed new methods for identifying and extracting the upwelling region along the Moroccan coast from physical and biological satellite observations.

On the other side, authors in [19] calculated the upwelling index using Ekman's theory of wind stress mass transport. They presented and discussed the seasonal, annual, and interannual variability of upwelling activity at three selected stations along the Atlantic coast of Morocco from 1967 to 2019. The evaluation of this variability was performed using the widely recognized Ekman Upwelling Index.

Other indices have also been proposed to quantify the intensity of coastal upwelling. For instance, authors in [20] developed an upwelling index called the "chlorophyll index" in order to investigate the variability of phytoplankton biomass across the entire Benguela ecosystem. This index is determined by the integration of the CHL-a concentration from the coastline to the limit of the extracted upwelling regions. Another study [21] developed a "velocity index" based on the dynamics of regional circulation and cross-shore density structure. Also, authors in [22] combined advanced very high-resolution radiometer (AVHRR) sea surface temperature (SST) and ERS-2 scatterometer wind stress data to create another metric dubbed "upwelling intensity".

On the other hand, several works have been carried out based on these indices in order to study Moroccan Atlantic coastal upwelling, which is the main object of this study. These studies suggested a stable and very active upwelling in summer in the northern area and a quasi-permanent and very active upwelling in spring, summer, and autumn between Cap Blanc and Cap Juby in the southern area [23,24]. Moreover, Ref. [25] shows that upwelling activity in the area appears in April, intensifies in June–August, and persists until October.

In addition to the prior research, the authors in [26,27] provided two distinct approaches based on an image fusion idea to detect Moroccan coastal upwelling. Indeed, they were able to identify the upwelling region from both SST and chlorophyll-*a* images, and they also offered a new index to evaluate their suggested approach.

However, monitoring coastal productivity is not an easy task due to the complex topography of the region and the limited resources that are available. To overcome these challenges, we have developed a new upwelling index specifically for the Moroccan Atlantic coast using SST images. This new tool can be used to understand the dynamics of the upwelling process and predict its future development. The new upwelling index incorporates the characteristics of upwelling intensity, such as nutrient availability, which allows for a more precise approach to quantifying upwelling dynamics. This information is crucial for assessing the relationship between upwelling intensity and the distribution and abundance of fish species [28], enabling the identification of areas of high productivity and optimal fishing grounds. Additionally, the new upwelling index provides insights into the spatial and temporal variability of upwelling, which directly influences the growth and distribution of phytoplankton [29]. By capturing the intensity of upwelling, the index offers a means to monitor and predict the occurrence of phytoplankton blooms along the Moroccan Atlantic coast, contributing to the understanding of ecosystem dynamics, the assessment of water quality, and the identification of potential harmful algal blooms that may impact marine organisms and fisheries [4]. We have applied our new upwelling index over a 40-year composite time series of SST satellite images. In this work, we will describe the development of the new upwelling index, study the data in terms of seasonal variability, and divide our system into sub-regions based on upwelling seasonality.

The paper is organized as follows: Section 2 introduces the region of interest and outlines the data used for this study. Section 3 elaborates on the methodology employed to identify upwelling regions and introduce the novel upwelling index. Section 4 presents the experimental results and analysis, followed by the conclusion.

## 2. Data and Area of Interest

Our research focuses on the Moroccan Atlantic coast, which stretches from 21°N to 36°N and 6°W to 19°W, where upwelling fluctuation is high and diverse throughout the year [3]. This region is illustrated in Figure 1 together with a climatological image of SST in the same area. The SST data are derived from the Group for High-Resolution Sea Surface Temperature (GHRSSST) multi-product satellite-based ensemble (GMPE), which is publicly available on the climate data store website <https://cds.climate.copernicus.eu/> (accessed on 29 May 2022) Figure 1. This dataset provides daily estimates of global sea surface temperature based on observations from multiple satellite sensors. The images used in this work were obtained by averaging the data from the previous eight days. We considered eight-day images because they allowed us to limit the number of pixels affected by clouds and to reduce the computational load by processing fewer images per day. In addition, this approach helped us balance the variability of pixel values and the need for continuous spatio-temporal coverage [2,30].

Each satellite image is represented by a 315 × 315 pixel map with a spatial resolution of 4 × 4 km. Our database contains 1778 eight-day SST images covering the time period from 1982 to 2021. Sea surface temperature provides a synoptic view of the temperature distribution of the skin (first micrometers of the surface layer) of the surface ocean [31]. Figure 2 shows an example of these products that were used in this work and demonstrates the

upwelling scenarios experienced during this investigation. The region in gray in Figure 2's SST image represents Moroccan land. The SST unit is expressed in degrees Celsius.

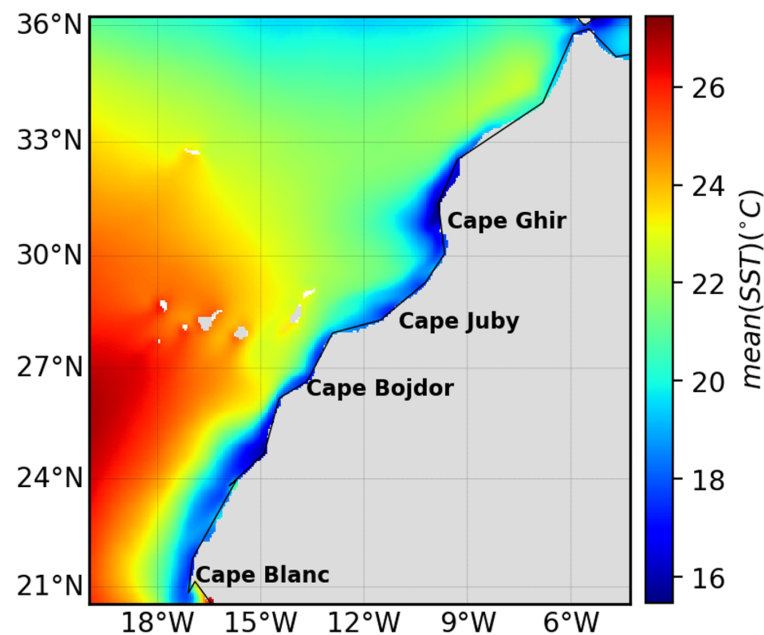


**Figure 1.** Climatological means of SST images over the Moroccan coast. Each pixel of the infrared image contains temperature information expressed in Celsius degrees ( $^{\circ}\text{C}$ ) between 1982 and 2021.

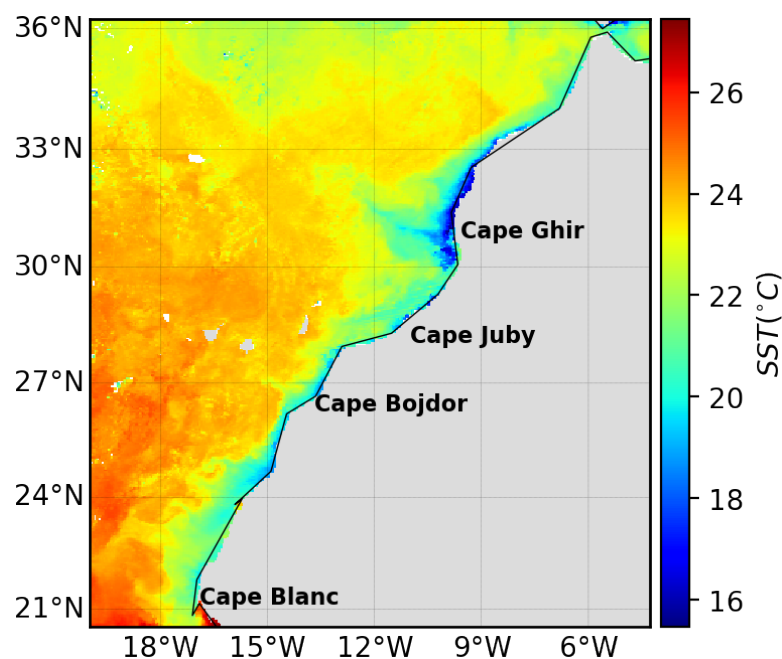


**Figure 2.** Example of eight-day SST image obtained in the first week of January 2007. Each pixel presents temperature in ( $^{\circ}\text{C}$ ). This image shows a typical upwelling scenario over the studied area.

The daily wind data for the period between 1987 and 2021 are provided from the QuikSCAT and ASCAT wind estimates with  $1/4^{\circ}$  resolution. These data are used to compute the Cross-Shore Ekman Transport index.

### 3. Materials and Methods

This work aims at proposing a new upwelling index based on the use of SST images to explore the interannual variability of upwelling along the Moroccan Atlantic coast. For

this purpose, we computed the new upwelling index and its anomalies. The computation of the proposed new upwelling index can be summarized in the following steps: first, we used the method developed in [18] to identify and extract upwelling areas from SST images and then we used the output to provide a new way of assessing upwelling dynamics.

### 3.1. Upwelling Extraction

In this work, we make use of the method developed in [18] to detect and track upwelling regions from SST images. This method can be summarized into the following steps:

#### 3.1.1. Ekman Preprocessing

The method described in [18] is primarily based on the Ekman theory, which is the main driver of the upwelling phenomenon. As described in [32], the movement of surface water to the right of the wind direction, caused by Ekman transport, can result in coastal upwelling in certain regions such as the northwest African margin. Therefore, to detect the occurrence of upwelling, it is common practice to compare the temperature of coastal water with offshore water. To incorporate this information into the preprocessing stage, a meridional normalization of SST images was proposed in [18]. This normalization involves dividing the image into perpendicular lines along the coastline (the black line in Figure 3) and comparing the temperature of coastal water with offshore water. Each line was normalized by dividing its temperature pixels by the maximal temperature observed in the offshore region. This normalization step improved the identification of upwelling areas and preserved the thermal structures of the original SST image. Additionally, a moving average algorithm was applied to mitigate fluctuations in the vector of maximal temperatures. The resulting normalized image (Figure 4a) exhibited clear distinctions between offshore and coastal information, enhancing the visualization and analysis of upwelling.

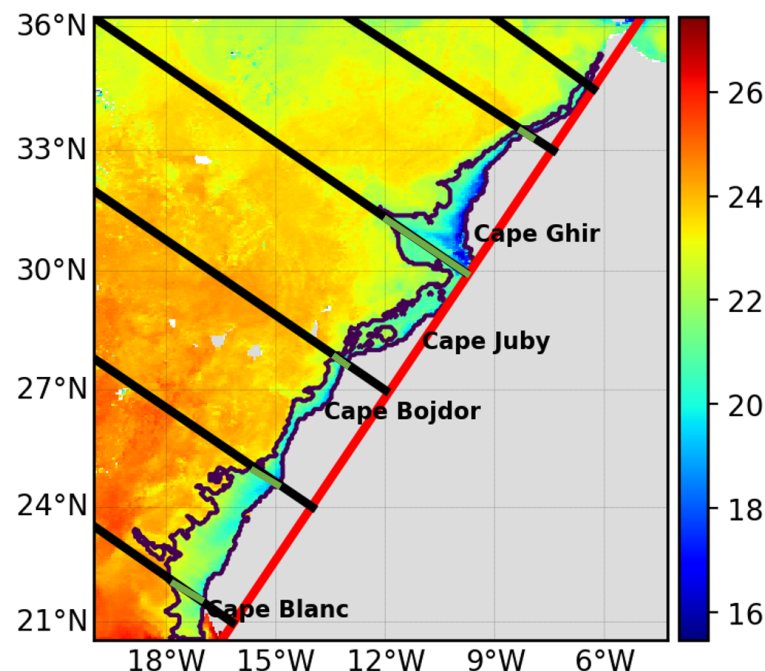
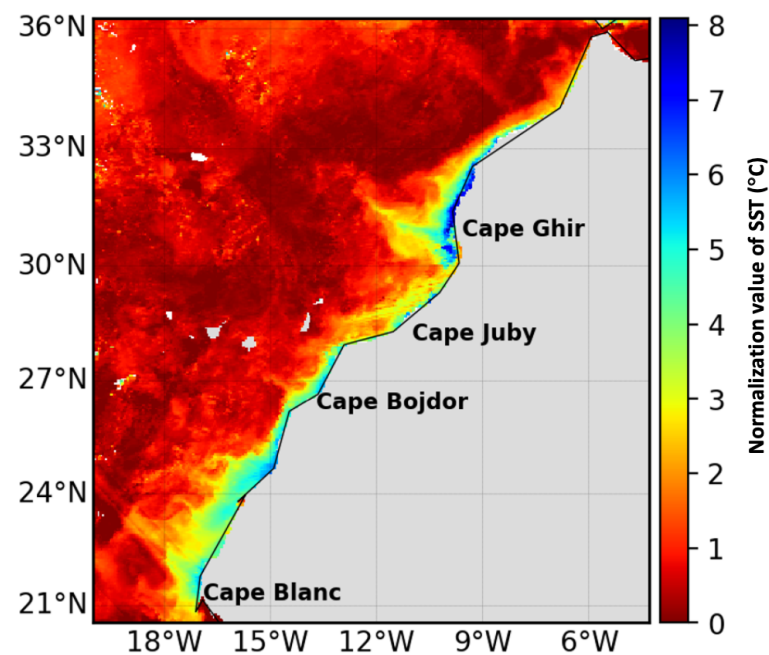


Figure 3. Example of the configuration used to compute the upwelling indices.



(a)



(b)

**Figure 4.** (a) Normalization applied to the SST image in Figure 2. (b) The binary outcome resulting from applying FCM and region-growing algorithms to the normalized SST image in (a). The white color in (b) is used to represent upwelling water, while the black color in (b) denotes offshore water [18].

### 3.1.2. Segmentation

Once the images are normalized, the method proceeds by applying the FCM algorithm. FCM is a clustering algorithm that assigns each data point to one or more clusters based on their degree of membership. The algorithm calculates the centroid of each cluster and adjusts the membership degrees iteratively to minimize the objective function, which represents the sum of squared differences between each data point and the centroid of its assigned cluster. Then, this algorithm is applied with two classes to separate the

cold, nutrient-rich water from the warmer water in the offshore. Then, a region-growing algorithm is made use of. The region-growing algorithm is used to merge neighboring pixels with those inside the region based on homogeneity and adjacency criteria in order to remove offshore noise and, finally, extract the upwelling region, as shown in (Figure 4b).

We must mention that the segmentation method developed in [18] allows us to identify the upwelling region from SST images on the entire Atlantic coast of Morocco.

### 3.2. New Upwelling Index

#### 3.2.1. Setup

Coastal upwelling is conditioned by the width of its continental shelf. For this reason, the radials are drawn perpendicular (black line in Figure 3) to the general direction of the coast which is represented by a virtual line (red line in Figure 3).

#### 3.2.2. New Upwelling Index Calculation

In the literature, the coastal upwelling index ( $CUI_{SST}$ ) is defined as a simple thermal difference between warmer offshore waters and the cold coastal water at the same latitude to analyze the seasonal and interannual variability of the upwelling intensity [2,8,12,14,16]. The general formulation of  $CUI_{SST}$  is as follows:

$$CUI_{SST} = SST_{max} - SST_{min} \quad (1)$$

where  $SST_{min}$  represents the minimum temperature between the coast and the continental slope, and  $SST_{max}$  represents the offshore temperature.

Authors in [2] determine the upwelling index as

$$I^r = T_{max}^r - T_{min}^r \quad (2)$$

where  $T_{max}^r$  and  $T_{min}^r$  are, respectively, the maximal offshore and minimal inshore temperatures. The results of the upwelling index developed in [2] ( $I^r$ ) from SST are shown via a space–time Hövmoller diagram over the period between 1982 and 2021 (Figure 5b).

The new upwelling index is computed as a thermal difference between the maximum temperature value within the upwelling and the cool upwelling water encountered along the same radial over the extracted upwelling region.

$$I_{sst_{up}}^r = SST_{max}^{up} - SST_{min}^{up} \quad (3)$$

#### 3.2.3. $SST_{max}^{up}$ , $SST_{min}^{up}$ Identification

The most commonly used approach is to consider  $SST_{min}$  as the minimum temperature between the coast and the continental slope, while  $SST_{max}$  is the offshore temperature. Authors in [8] opted to choose  $SST_{min}$  between the coast and the 200 m depth contour and set  $SST_{max}$  at 500 km from the coast. On the other hand, Ref. [15] selected  $SST_{min}$  between 20 km and 40 km of the coastal region, while  $SST_{max}$  was found to be between 400 and 1000 km offshore. In [12], the authors performed a statistical study on a 30-year SST database to determine  $SST_{min}$ . They averaged it with the eight pixels surrounding the exact location of the minimum to minimize local noise in the data. For  $SST_{max}$ , they extracted it up to 3000 km in the offshore direction. Meanwhile, authors in [2] defined  $SST_{min}$  as the minimum temperature inside the extracted upwelling zone, while  $SST_{max}$  was defined similarly to [12], (i.e., the maximum temperature outside the extracted upwelling zone up to 3000 km offshore). Figure 5b presents a space–time Hövmoller plot of the seasonal and interannual variability of the  $I_r$  from 1982 to 2021, as developed by [2].

Our study proposes a novel approach for identifying  $SST_{max}$  and  $SST_{min}$  by leveraging the results of the upwelling extraction method described in Section 3.1 In contrast to previous methods that only search for  $SST_{min}$  within a fixed band from the coast, our new upwelling index chooses  $SST_{min}$  as the minimum temperature within the upwelling zone. This ensures that all the necessary low temperatures are taken into account for a

more comprehensive calculation. Additionally, we determine  $SST_{max}$  as the maximum temperature within the upwelling zone, this eliminates any arbitrary choice of position and focuses solely on the upwelling region.

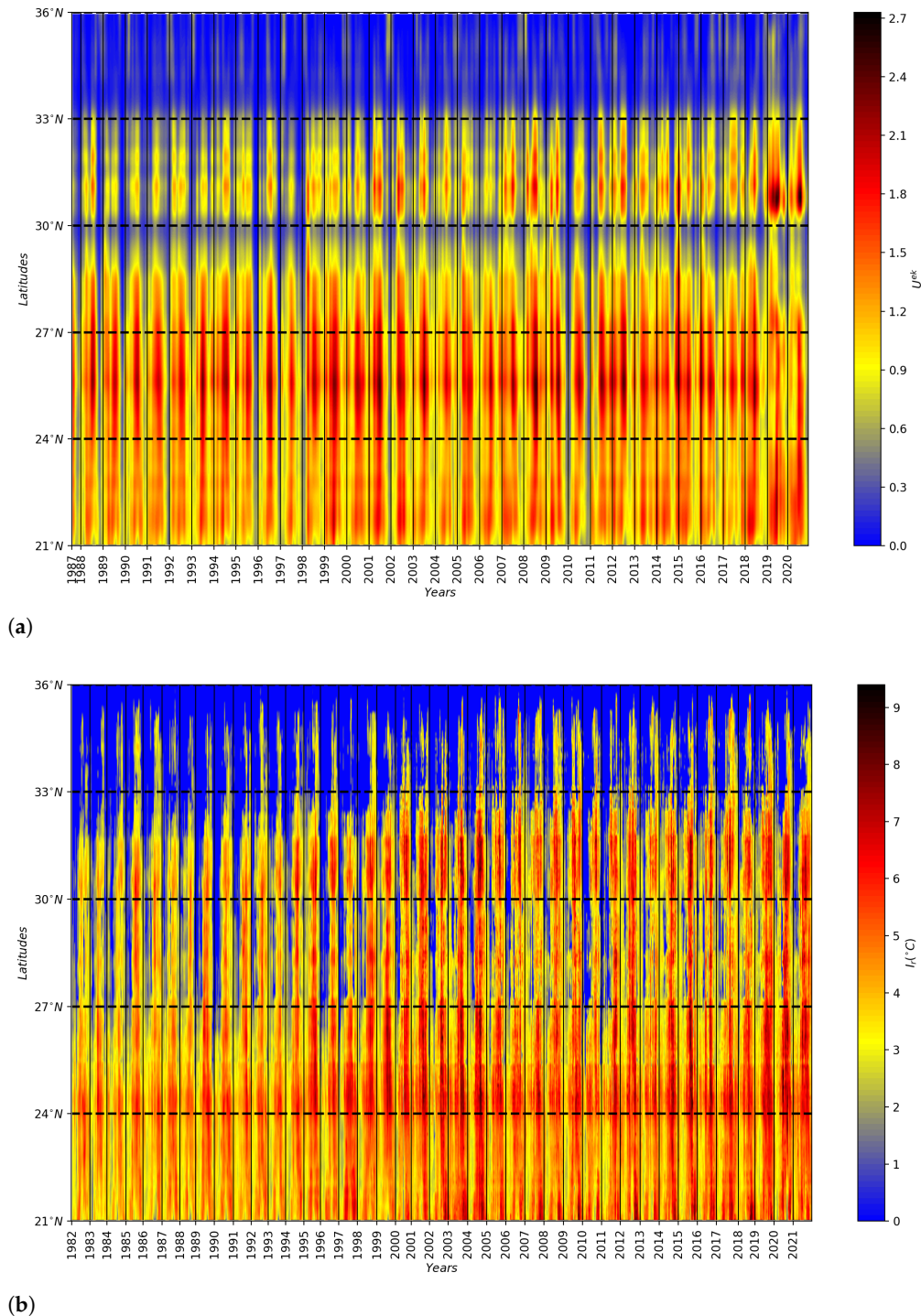


**Figure 5.** Space–time Hövmoller diagram: (a) Cross-Shore Ekman Transport ( $I_E$ ) and (b) upwelling index ( $I'$ ) developed by [2] over the period between 1982 and 2021.

Thus,  $SST^{upmax}$  and  $SST^{upmin}$  represent, respectively, the highest and lowest coastal temperatures within the upwelling zone (Figure 6).

Thus, starting from north to south (Figure 3), each segmented upwelling region  $S_{up} \in \{1, \dots, \text{length}(\text{data})\}$  includes radials, and each radial  $r \in \{1, \dots, n\}$  contains temperature

values  $r = \{T_i^r; i = 1, \dots, n\}$ . Therefore, over each radial, the  $SST_{min}^{up}$  and  $SST_{max}^{up}$  are defined as

$$SST_{max}^{up} = \max_{S_{up}}(T_i^r) \quad (4)$$

$$SST_{min}^{up} = \min_{S_{up}}(T_i^r) \quad (5)$$

Figure 3 shows an example where we look for  $SST_{max}^{up}$  and  $SST_{min}^{up}$  (green color). The results of our new upwelling index calculation ( $I_{SST_{up}}^r$ ) from SST are shown via a space–time Hövmöller diagram over the period between 1982 and 2021 (Figure 6).

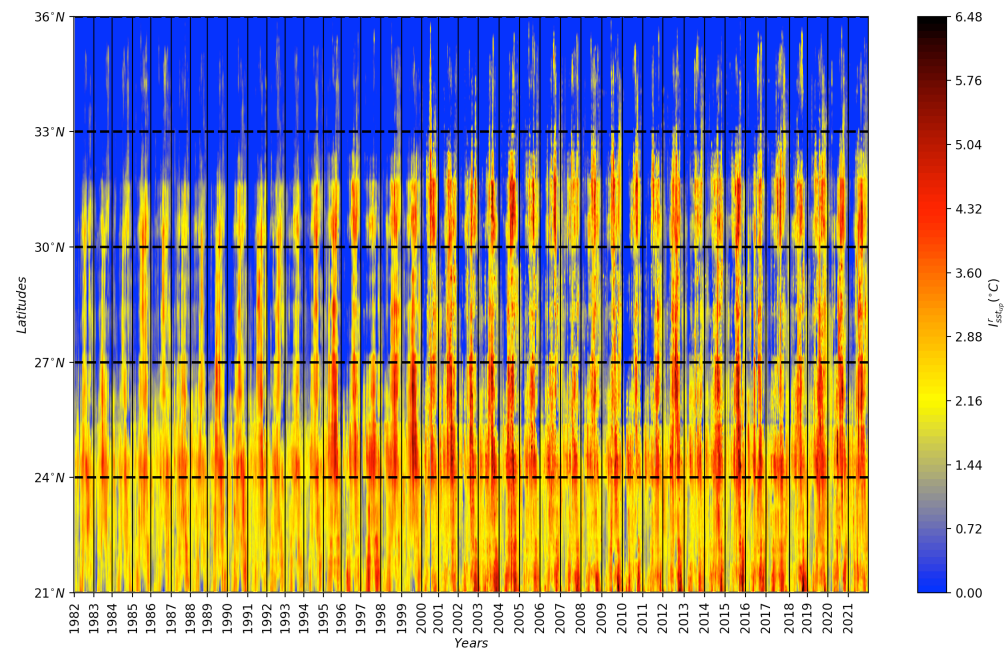


**Figure 6.** Space–time Hövmöller diagram of new upwelling index ( $I_{SST_{up}}^r$ ) from SST over the period between 1982 and 2021.

### 3.2.4. Ekman Transport Index

Wind-driven coastal upwelling is primarily influenced by the along-shore component of wind stress, which induces both offshore and onshore Ekman transport ( $I_E$ ) along the coast. The calculation of Ekman transport involves the utilization of daily wind measurements.

To quantify Ekman transport, we start by obtaining the meridional wind stress ( $\tau_y$ ) from available wind data. This component represents the force per unit area exerted by the wind in the north–south direction.

The Ekman transport index ( $I_E$ ) is then determined using the following equation:

$$I_E = \frac{\tau_y}{\rho f} \quad (6)$$

This equation expresses the ratio of the meridional wind stress ( $\tau_y$ ) to the product of seawater density ( $\rho$ ) and the Coriolis parameter ( $f$ ). The resulting index, expressed in units of  $m^2 \cdot s^{-1}$ , serves as an indicator of coastal upwelling intensity.

By incorporating this calculation of Ekman transport, we can assess the magnitude and direction of coastal upwelling along the Moroccan Atlantic coast. The calculated Ekman transport values contribute to the overall upwelling index, providing valuable insights into the dynamics and variability of upwelling in the study region. The results of the Ekman transport index ( $I_E$ ) are shown via a space–time Hövmöller diagram over the period between 1987 and 2021 (Figure 5a).

### 3.2.5. Anomalies

- Spatial anomalies are calculated as the difference between the new upwelling index values and its corresponding mean values for each image. A positive spatial anomaly suggests an anomalous increase in upwelling activity for that period. Conversely, a negative spatial anomaly indicates an anomalous decrease in upwelling activity (Figure 7a).
- The temporal anomalies are determined as the difference between the new upwelling index value and its corresponding mean value for each latitude. A positive temporal anomaly suggests an anomalous increase in upwelling activity at a latitude. Conversely, a negative temporal anomaly indicates an anomalous decrease in upwelling activity. This could indicate weaker upwelling or deviations from typical seasonal patterns (Figure 8a).

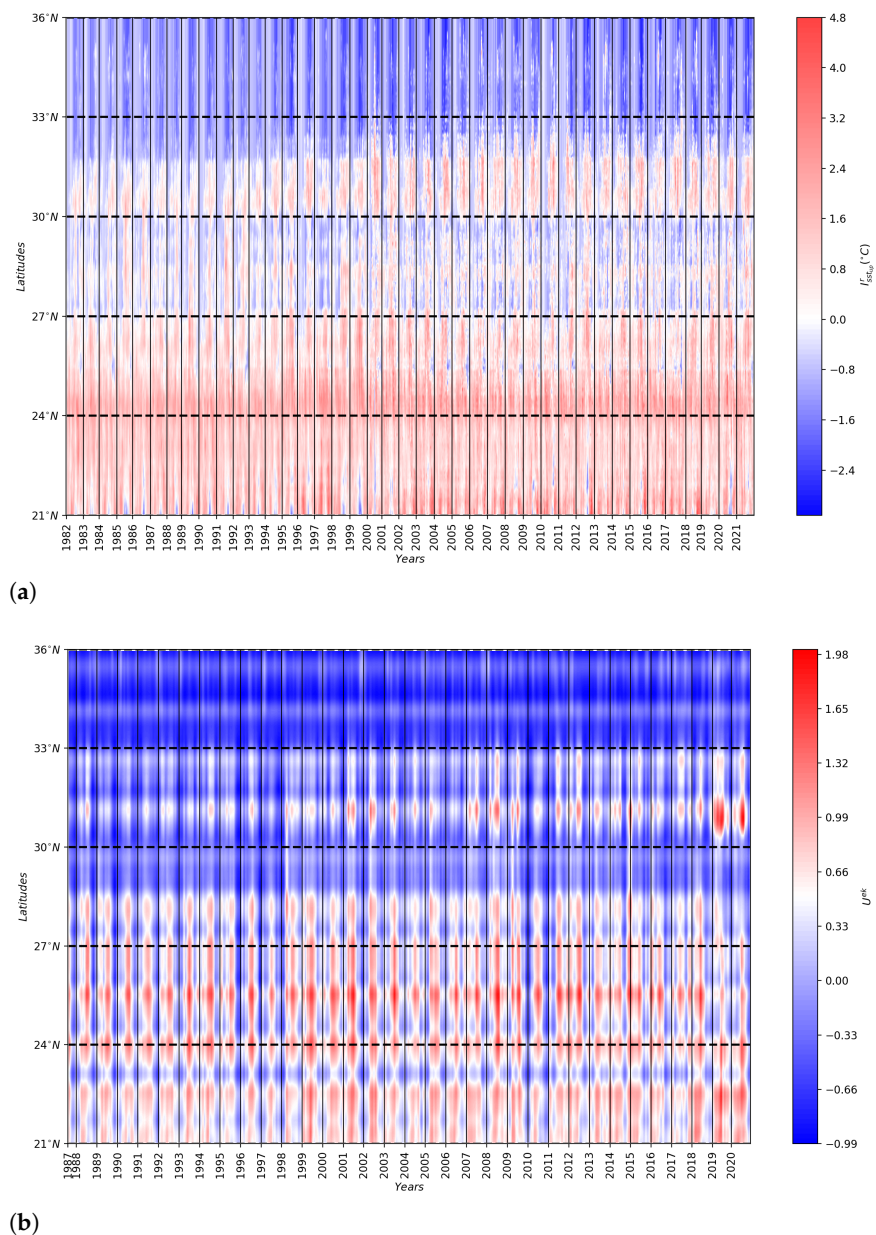


**Figure 7.** Space–time Hövmöller diagram presenting spatial anomalies of (a) new upwelling index ( $I_{sst_{up}}^r$ ) and (b) Cross-Shore Ekman Transport ( $I_E$ ) over the period between 1982 and 2021.

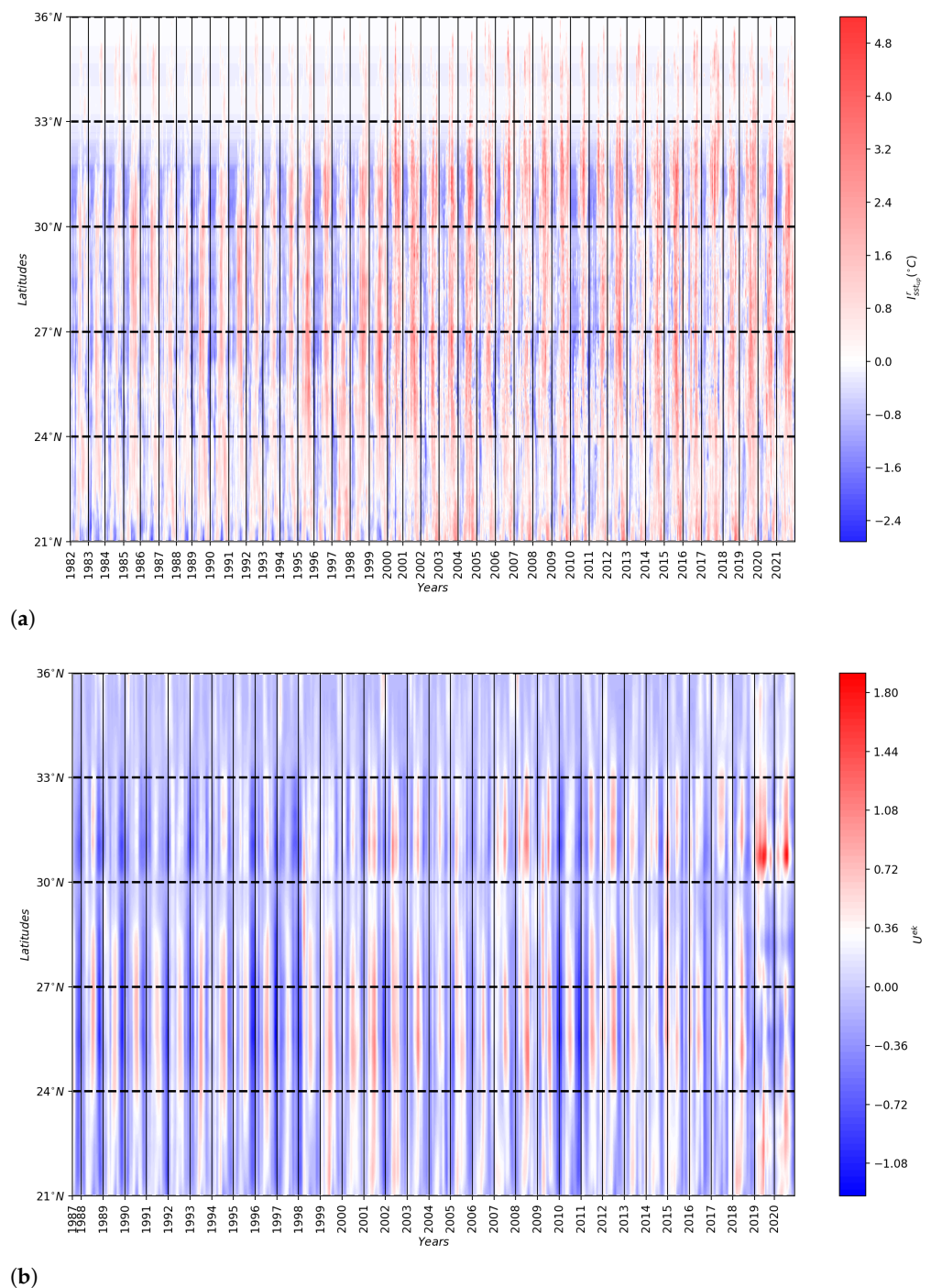


**Figure 8.** Space–time Hövmoller diagram presenting temporal anomalies of (a) new upwelling index ( $I_{sst_{up}}^r$ ) and (b) Cross-Shore Ekman Transport ( $I_E$ ) over the period between 1982 and 2021.

## 4. Discussion

### 4.1. SST Upwelling Index

The proposed new upwelling index is employed to generate and demonstrate the seasonal and interannual variability of the Moroccan upwelling and their anomalies using Hövmoller diagrams at a 4 km/8-day spatio-temporal resolution computed from SST between 21°N and 36°N over the period 1982–2021 (Figures 6–8). The spatio-temporal variability of our new upwelling index ( $I_{sst_{up}}^r$ ) is compared to the Cross-Shore Ekman Transport index ( $I_E$ ) and the old upwelling index ( $I_r$ ) calculated over the same period (Figure 5a,b).

The new SST upwelling index varies from 0 degrees to 6.5 degrees. The primary upwelling patterns derived from physical and biological observation are largely the same, and they are very similar to the Cross-Shore Ekman Transport (Figure 5a). This agreement with the wind-based upwelling index confirms our novel upwelling index and enables further analysis of sub-mesoscale oscillations that the new upwelling index does record but are not caught by the wind. According to our new upwelling index, our system can be synthesized into three distinct zones:

- The northern area, bounded by 33°N and 36°N, shows the lowest temperatures along the coast throughout the 40-year time series in contrast to what was observed in Figure 5b. These low values are due to the weaker winds and unfavorable coastline orientation in this region (winds are not parallel to the coastline) [2] (Figures 5a and 6).
- Central part between 27°N and 33°N: The giant filament around Cape Ghir is primarily responsible for the increased upwelling index in this zone. In Figure 5b, we notice an absence of upwelling in winter. Our new index (Figure 6) reveals distinct patterns. It indicates the absence of upwelling during winter, and there are also intermittent periods in spring and summer when no upwelling is observed. Notable periods where upwelling is absent are 1989–1997, 2005, 2010–2011, as well as 2013 and 2017. Globally, the  $I_{sst_{up}}^r$  in the central part has significant upwelling all year round. In fact, the areas with the greatest intensity values (3°C to 5°C) are noted at 28°N, 29°N, 31°N, and 32°N, respectively, where considerable upwelling filaments have occurred [33]. The focus shifts to the  $I_E$  to analyze the interannual and seasonal fluctuation of upwelling intensity (Figure 5a). Globally, the patterns of  $I_{sst_{up}}^r$  and  $I_E$  show a good relationship. In fact, between April and November of most years, the primary wind pattern favorable to upwelling in the central zone was primarily between latitudes 28°N and 31°N.
- Southern part between 21°N and 27°N: The interannual and seasonal thermal variability of the upwelling indicates that upwelling in this area is generally strong, according to Figure 5b, and remains so throughout the year. However, our analysis reveals that while upwelling is generally stronger in this region, it is not as consistent or intense during all seasons. Indeed, upwelling activity is strong and continuous between 24°N and 26°N throughout the years, with maximum values of  $I_{sst_{up}}^r$ , especially from summer to autumn (Figure 6). In contrast, it is absent or average in all winters. The intensity in  $I_{sst_{up}}^r$  is greatest from spring to autumn, with temperatures in the south between 3 and 6 degrees Celsius, which corresponds to the strong trade winds that blow near the shore (Figure 5a). The presence of upwelling revealed several intriguing discontinuities, especially near 27°N. Indeed, it is not present every year from June to September (Figure 6). A decrease in the new upwelling index was observed in the years 1990–1996 and 2010–2011, and this can be attributed to the extremely negative values of the North Atlantic Oscillation. Overall, the  $I_{sst_{up}}^r$  and  $I_E$  models are similar, indicating the effectiveness of assessing upwelling intensity as the radial thermal difference between the minimum and maximum of coastal temperatures.

By comparing our new upwelling index (Figure 6) to the one developed in [2] (Figure 5b) and to the Cross-Shore Ekman Transport index (Figure 5a), we found that ours provides a more accurate representation of upwelling dynamics. On a large scale, it is clear that our new upwelling index,  $I_{sst_{up}}^r$ , is much closer to  $I_E$  than to  $I_r$ . In addition,  $I_{sst_{up}}^r$  and  $I_E$  have nearly identical seasons of high and low values in the three regions analyzed. However, on a smaller scale,  $I_r$  has high intensity throughout the year in the southern region between 21°N and 27°N, whereas  $I_{sst_{up}}^r$  and  $I_E$  have significantly lower intensity in winter and spring. In the central region, between 27°N and 33°N,  $I_r$  has a moderate intensity near 30°N, while  $I_{sst_{up}}^r$  and  $I_E$  have a very low intensity. The largest difference in intensity is seen in the northern region between 33°N and 36°N, where  $I_r$  is relatively high, although there is a near absence of upwelling in this area. Conversely,  $I_{sst_{up}}^r$  and  $I_E$  exhibit the expected lack of intensity in this region.

In summary, our new upwelling index shows average upwelling intensity in three zones. Indeed, upwelling intensity decreases from south to north, with temperatures ranging from about 3 °C to 6.5 °C in the southern region, from 2 °C to 4.5 °C in the central region, and below 1 °C in the northern region throughout the year. In addition, the seasonal variability shows a notable pattern: upwelling is low or non-existent in winter and gradually increases in intensity throughout the year, reaching its maximum in summer.

#### 4.2. Interannual Variability of the Upwelling Dynamics from SST Images

To better study upwelling activity, we present our new upwelling index  $I_{sst,up}^r$  at three sites (24°N, 29°N, and 31°N). Figure 9 displays the interannual variations in the upwelling activity at the three selected sites mentioned above from 1982 to 2021. Based on these results, we observe that the three latitudes follow a general trend during each year that the maximum activity peaks are recorded.

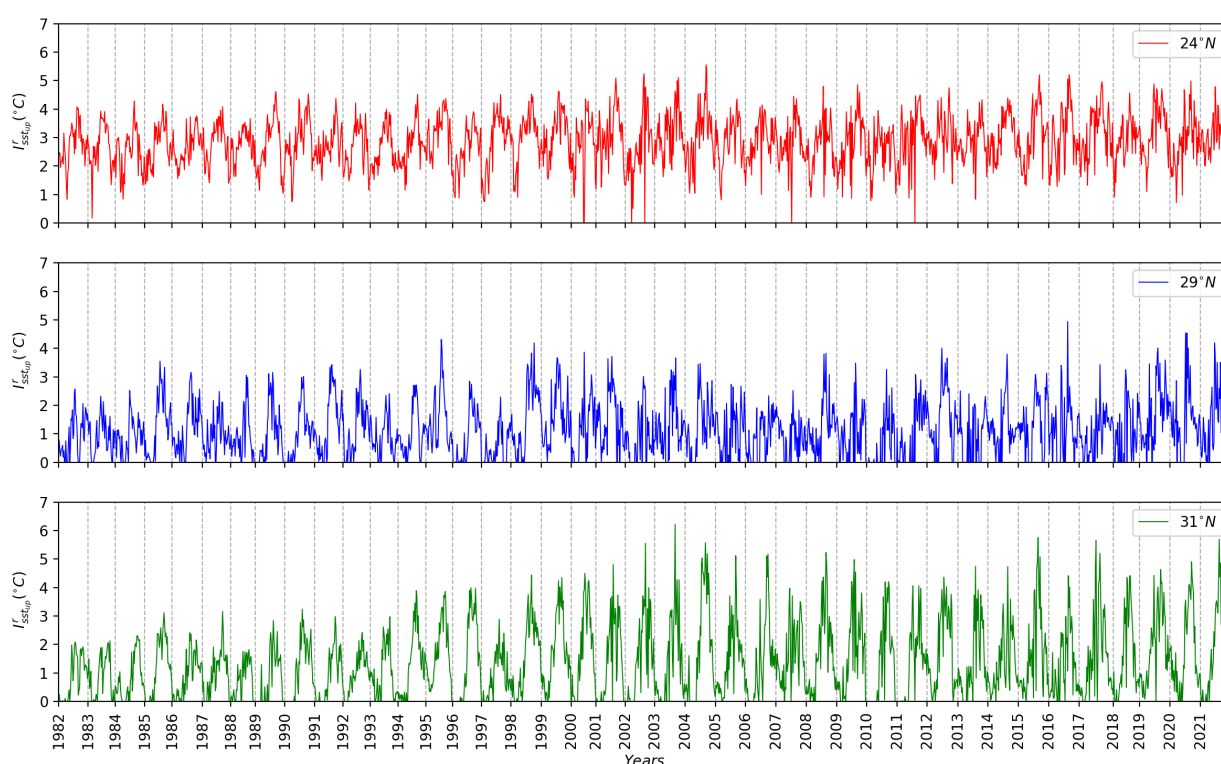


**Figure 9.** New upwelling index ( $I_{sst,up}^r$ ) at the three selected stations over the years 1982–2021: 24°N (red color), 29°N (blue color), and 31°N (green color).

Latitude 24°N, which represents the southern part of Morocco, has higher activity than the other latitudes (29°N and 31°N) in this region, which are located in the northern part. In summer, there is a strong upwelling activity on the latitude of 24°N, especially from 2001 to 2004 and from 2015 to 2017, when the upwelling index is maximum (exceeds 5 degrees) (Figure 9). Average upwelling activity was observed in the years 1982 to 1989, 2005 and 2010 in the same season. The lowest upwelling index minimums at this latitude were recorded in autumn and winter in the years 2000, 2002, 2007, and 2011 (Figure 9).

The strongest upwelling activities are observed in the summer for the latitude 29°N, with an upwelling index that is maximum (between 4 and 5 degrees) in the years 1995, 1998, 2012, 2016, and 2019 to 2021 (Figure 9). Upwelling activity is low during the autumn and winter seasons on the same latitude where the strongest minimum upwelling index values were observed over the years 1982–1985, 1996–1998, 2006–2007, and 2013 (Figure 9).

The most significant upwelling activities (maximum upwelling index exceeding 5 degrees) are observed in the summer season at the latitude of 31°N over the periods

2002–2006, 2008–2009, 2015, 2017, and 2021 (Figure 9). In contrast, low upwelling activity is visible in winter in the years 1982–1985, 1988, and 1992 (Figure 9).

We can conclude from these three stations that the interannual variability of the upwelling has strong seasonal dynamics of the upwelling activity along Morocco's Atlantic coast. This indicates that the intensity and occurrence of upwelling events vary significantly throughout the year. Furthermore, there is a noticeable increase in upwelling activity from north to south along the coast, aligning with the pattern of upwelling seasonality. The southern regions experience a more pronounced and quasi-permanent upwelling, characterized by consistently high values. On the other hand, the northern part of the coast exhibits a decrease in the upwelling index, suggesting a higher influence of non-upwelling processes in this area. These findings indicate that the upwelling phenomenon is not solely driven by seasonal factors but is also influenced by additional processes that impact biological productivity. One such factor could be the presence of mesoscale instabilities, which can influence the distribution and intensity of upwelling events [19]. Additionally, the activities of marine life in the region may contribute to variations in upwelling patterns and associated productivity. These results highlight the presence of distinct oceanographic and climatic characteristics between the northern and southern parts of the study area. This suggests that the southern region may have a more favorable environment for upwelling, leading to enhanced biological productivity, while the northern region is more susceptible to non-upwelling processes that can limit upwelling-related benefits.

#### 4.3. Interannual Variability of the $I_{sst,up}^r$ and $I_E$ Anomalies

A more detailed space–time Hövmoller diagram of spatial and temporal anomalies from 1982 to 2021 is presented in Figures 7 and 8.

The interannual variability of spatial and temporal anomalies in the upwelling index  $I_{sst,up}^r$  along the Atlantic coast of Morocco provides an insight into annual fluctuations in upwelling intensity and patterns. By analyzing changes in anomalies, we can observe the variability of upwelling conditions over time. Spatial and temporal analysis reveals a succession of years of high and low upwelling intensity throughout the study period (Figures 7 and 8). Significant interannual variability is observed, indicating periods of high and low upwelling along the coast.

We can see that the years 1995–1996, 1998–2009, and 2012–2021 have significant vertical velocity transport, corresponding to stronger periods in the  $I_{sst,up}^r$  records. These pronounced anomalies are linked to the collapse of the regional sardine stock between 1996 and 1997 and a very low number of juveniles in 1996 and 1998 [34] ( Figures 8a and 9). Conversely, some years show abnormally low yields (Figure 8a). The years 1983 to 1994 and 2010 to 2011 stand out as periods of weaker upwelling intensity with exceptionally low winds (Figure 8b). In addition, a distinct zone of very weak upwelling is identified between 26°N and 33°N during the years 1996 to 1997 and 2010 to 2011. This weak upwelling is attributed to an exceptional easing of the trade winds during these periods, as shown by Ekman's cross-shore transport data (Figure 8b) [16].

The spatial distribution of upwelling anomalies shows marked variability along the Moroccan coast (Figure 7a). The southern part consistently experiences higher upwelling intensity than other regions. Anomalies in this region suggest a persistent pattern of strong upwelling, specifically in the summer months (June to September), which tend to experience stronger winds along the Moroccan coast (Figure 7b). These winds are often associated with the intensification of the trade winds. Moving towards the central part of the coast, between 27°N and 33°N, we observe intermediate levels of upwelling intensity (Figure 7a), although they are not as pronounced as in the southern region. More practically, the spring (March to May) and autumn (October to November) seasons can be marked by a weakening of the trade winds (Figure 7b). These periods can be marked by relatively weaker winds, resulting in reduced upwelling intensity along the coast. In contrast, the northern part of the Moroccan coast shows little or no upwelling, indicating weak or sporadic upwelling and relatively low upwelling intensity. The interannual variability of spatial and temporal

anomalies highlights the dynamic nature of upwelling along Morocco's Atlantic coast. These fluctuations can have an impact on the productivity and distribution of marine organisms, including fish populations and phytoplankton blooms.

## 5. Conclusions

We proposed a new upwelling index based on both physical and biological observations, to study the upwelling activity along the Moroccan Atlantic coast spanning from 21°N to 36°N and 6°E to 19°E. This new upwelling index is calculated from a recent method that takes into account the physics at the origin of the phenomenon, which allows a better understanding of its dynamics and has high accuracy in the detection of upwelling. Two upwelling indices, namely, "new upwelling index" ( $I_{sstup}^r$ ) and "Ekman transport" ( $I_E$ ) and their spatial and temporal anomalies were used in our analysis, which was calculated at each latitude and at each time step of the interannual variability. These indices were computed over a period of 40 years of satellite images to study and analyze the upwelling activity in the Moroccan region. We divided our system into three sub-regions characterized by different properties. We compared our new upwelling index to the one developed in a previous study [2] and the Ekman Transport index and found that ours provides a notably more precise portrayal of the dynamics. Additionally, unlike the other index, our new upwelling index is more effective in analyzing upwelling and can be used at any time resolution. Furthermore, the technique we devised in this work can be effortlessly customized to examine upwelling in other regions worldwide. Then, we selected three sites (24°N, 29°N, and 31°N) from the new upwelling index to better understand the periods of low and high upwelling activity. We also evaluated the effectiveness of each satellite observation on each sub-region in order to make better recommendations for monitoring and tracking upwelling.

**Author Contributions:** Conceptualization, K.M. and A.E.A.; methodology, H.B., K.M. and A.E.A.; software, H.B., K.M. and A.E.A.; validation K.M., A.E.A. and K.H.; formal analysis, H.B., K.M. and A.E.A.; investigation, K.M., R.S. and A.C.; resources, K.M., R.S. and A.C.; writing—original draft preparation, H.B.; writing—review and editing, H.B., K.M. and A.E.A.; visualization, H.B.; supervision, K.M. and A.E.A.; project administration, K.M. All authors have read and agreed to the published version of the manuscript.

**Funding:** This research received no external funding.

**Data Availability Statement:** Not applicable.

**Conflicts of Interest:** The authors declare no conflict of interest.

## References

1. Tamim, A.; Minaoui, K.; Daoudi, K.; Yahia, H.; Atillah, A.; El Fellah, S.; Aboutajdine, D.; El Ansari, M. Automatic detection of Moroccan coastal upwelling zones using sea surface temperature images. *Int. J. Remote Sens.* **2019**, *40*, 2648–2666. [[CrossRef](#)]
2. El Aouni, A.; Garçon, V.; Sudre, J.; Yahia, H.; Daoudi, K.; Minaoui, K. Physical and biological satellite observations of the northwest african upwelling: Spatial extent and dynamics. *IEEE Trans. Geosci. Remote Sens.* **2019**, *58*, 1409–1421. [[CrossRef](#)]
3. Tamim, A.; Minaoui, K.; Daoudi, K.; Yahia, H.; Atillah, A.; Aboutajdine, D. An efficient tool for automatic delimitation of Moroccan coastal upwelling using SST images. *IEEE Geosci. Remote Sens. Lett.* **2014**, *12*, 875–879. [[CrossRef](#)]
4. Pitcher, G.; Figueiras, F.; Hickey, B.; Moita, M. The physical oceanography of upwelling systems and the development of harmful algal blooms. *Prog. Oceanogr.* **2010**, *85*, 5–32. [[CrossRef](#)] [[PubMed](#)]
5. Vinayachandran, P.N.M.; Masumoto, Y.; Roberts, M.J.; Huggett, J.A.; Halo, I.; Chatterjee, A.; Amol, P.; Gupta, G.V.; Singh, A.; Mukherjee, A.; et al. Reviews and syntheses: Physical and biogeochemical processes associated with upwelling in the Indian Ocean. *Biogeosciences* **2021**, *18*, 5967–6029. [[CrossRef](#)]
6. Bakun, A. Global climate change and intensification of coastal ocean upwelling. *Science* **1990**, *247*, 198–201. [[CrossRef](#)] [[PubMed](#)]
7. Demarcq, H.; Faure, V. Coastal upwelling and associated retention indices derived from satellite SST. Application to Octopus vulgaris recruitment. *Oceanol. Acta* **2000**, *23*, 391–408. [[CrossRef](#)]
8. Nykjær, L.; Van Camp, L. Seasonal and interannual variability of coastal upwelling along northwest Africa and Portugal from 1981 to 1991. *J. Geophys. Res. Ocean.* **1994**, *99*, 14197–14207. [[CrossRef](#)]

9. Wooster, W.S.; Bakun, A.; McLain, D.R. The seasonal upwelling cycle along the eastern boundary of the North Atlantic. 1976. *J. Marine Res.* **1976**, *34*. Available online: [https://elischolar.library.yale.edu/journal\\_of\\_marine\\_research/1351](https://elischolar.library.yale.edu/journal_of_marine_research/1351) (accessed on 1 March 2023).
10. Jacox, M.G.; Edwards, C.A.; Hazen, E.L.; Bograd, S.J. Coastal upwelling revisited: Ekman, Bakun, and improved upwelling indices for the US West Coast. *J. Geophys. Res. Ocean.* **2018**, *123*, 7332–7350. [[CrossRef](#)]
11. Chen, C.C.; Shiah, F.K.; Chung, S.W.; Liu, K.K. Winter phytoplankton blooms in the shallow mixed layer of the South China Sea enhanced by upwelling. *J. Mar. Syst.* **2006**, *59*, 97–110. [[CrossRef](#)]
12. Benazzouz, A.; Mordane, S.; Orbi, A.; Chagdali, M.; Hilmi, K.; Atillah, A.; Pelegrí, J.L.; Hervé, D. An improved coastal upwelling index from sea surface temperature using satellite-based approach—The case of the Canary Current upwelling system. *Cont. Shelf Res.* **2014**, *81*, 38–54. [[CrossRef](#)]
13. El Abidi, Z.; Minaoui, K.; El Aouni, A.; Tamim, A.; Laanaya, H. An efficient detection of moroccan coastal upwelling based on fusion of chlorophyll-a and sea surface temperature images with a new validation index. *IEEE Geosci. Remote Sens. Lett.* **2020**, *18*, 1322–1326. [[CrossRef](#)]
14. Van Camp, L.; Nykjaer, L.; Mittelstaedt, E.; Schlittenhardt, P. Upwelling and boundary circulation off Northwest Africa as depicted by infrared and visible satellite observations. *Prog. Oceanogr.* **1991**, *26*, 357–402. [[CrossRef](#)]
15. Santos, A.M.P.; Kazmin, A.S.; Peliz, A. Decadal changes in the Canary upwelling system as revealed by satellite observations: Their impact on productivity. *J. Mar. Res.* **2005**, *63*, 359–379. [[CrossRef](#)]
16. Benazzouz, A.; Demarcq, H.; González-Nuevo, G. Recent changes and trends of the upwelling intensity in the Canary Current Large Marine Ecosystem. *Oceanographic and Biological Features in the Canary Current Large Marine Ecosystem*. 2015. pp. 321–330. Available online: <https://aquadocs.org/handle/1834/9198> (accessed on 1 March 2023).
17. El Aouni, A.; Minaoui, K.; Tamim, A.; Daoudi, K.; Yahia, H. An improved method for accurate computation of coastal upwelling index using sea surface temperature images. In Proceedings of the 2018 9th International Symposium on Signal, Image, Video and Communications (ISIVC), Rabat, Morocco, 27–30 November 2018; pp. 76–81.
18. El Aouni, A.; Daoudi, K.; Minaoui, K.; Yahia, H. Robust detection of the North-West African upwelling from SST images. *IEEE Geosci. Remote Sens. Lett.* **2020**, *18*, 573–576. [[CrossRef](#)]
19. Hilmi, K.; Bessa, I.; Makaoui, A.; Houssa, R.; Idrissi, M.; Ettahiri, O.; EL Aouni, A. Long Term Upwelling Activity along the Moroccan Atlantic Coast. *Front. Sci. Eng.* **2021**, *11*.
20. Demarcq, H.; Barlow, R.; Hutchings, L. Application of a chlorophyll index derived from satellite data to investigate the variability of phytoplankton in the Benguela ecosystem. *Afr. J. Mar. Sci.* **2007**, *29*, 271–282. [[CrossRef](#)]
21. Thomson, R.E.; Ware, D.M. A current velocity index of ocean variability. *J. Geophys. Res. Ocean.* **1996**, *101*, 14297–14310. [[CrossRef](#)]
22. Kuo, N.J.; Zheng, Q.; Ho, C.R. Satellite observation of upwelling along the western coast of the South China Sea. *Remote Sens. Environ.* **2000**, *74*, 463–470. [[CrossRef](#)]
23. Makaoui, A.; Orbi, A.; Hilmi, K.; Zizah, S.; Larissi, J.; Talbi, M. L’upwelling de la côte atlantique du Maroc entre 1994 et 1998. *Comptes Rendus Geosci.* **2005**, *337*, 1518–1524. [[CrossRef](#)]
24. Bessa, I.; Makaoui, A.; Agouzouk, A.; Idrissi, M.; Hilmi, K.; Afifi, M. Variability of the ocean mixed layer depth and the upwelling activity in the Cape Bojador, Morocco. *Model. Earth Syst. Environ.* **2020**, *6*, 1345–1355. [[CrossRef](#)]
25. Bessa, I.; Makaoui, A.; Agouzouk, A.; Idrissi, M.; Hilmi, K.; Afifi, M. Seasonal variability of the ocean mixed layer depth depending on the cape Ghir filament and the upwelling in the Moroccan Atlantic coast. *Mater. Today Proc.* **2019**, *13*, 637–645. [[CrossRef](#)]
26. El Abidi, Z.; Minaoui, K.; Tamim, A.; Laanaya, H. Detection of Moroccan coastal upwelling using the alpha blending fusion technique of sea surface chlorophyll images and sea surface temperature images. In Proceedings of the 2018 4th International Conference on Advanced Technologies for Signal and Image Processing (ATSIP), Sousse, Tunisia, 21–24 March 2018; 2018; pp. 1–5.
27. Elabidi, Z.; Minaoui, K.; Tamim, A.; Laanaya, H. A simple fusion approach of chlorophyll images and sea surface temperature images for improving the detection of Moroccan coastal upwelling. In Proceedings of the IGARSS 2018–2018 IEEE International Geoscience and Remote Sensing Symposium, Valencia, Spain, 22–27 July 2018; pp. 7208–7211.
28. Kavanagh, L.; Galbraith, E. Links between fish abundance and ocean biogeochemistry as recorded in marine sediments. *PLoS ONE* **2018**, *13*, e0199420. [[CrossRef](#)] [[PubMed](#)]
29. Comesaña, A.; Fernández-Castro, B.; Chouciño, P.; Fernández, E.; Fuentes-Lema, A.; Gilcoto, M.; Pérez-Lorenzo, M.; Mouriño-Carballido, B. Mixing and phytoplankton growth in an upwelling system. *Front. Mar. Sci.* **2021**, *8*, 712342. [[CrossRef](#)]
30. Tamim, A.; Minaoui, K.; Daoudi, K.; Yahia, H.; Atillah, A.; Smiej, M.F.; Aboutajdine, D. A simple and efficient approach for coarse segmentation of Moroccan coastal upwelling. In Proceedings of the 21st European Signal Processing Conference (EUSIPCO 2013), Marrakech, Morocco, 9–13 September 2013; pp. 1–5.
31. Rayner, N.; Parker, D.E.; Horton, E.; Folland, C.K.; Alexander, L.V.; Rowell, D.; Kent, E.C.; Kaplan, A. Global analyses of sea surface temperature, sea ice, and night marine air temperature since the late nineteenth century. *J. Geophys. Res. Atmos.* **2003**, *108*. [[CrossRef](#)]
32. Ekman, V.W. On the Influence of the Earth’s Rotation on Ocean-Currents. *J. Arkiv Matematik Astronomi Och Fysik*. **1905**, Band 2 No 11. Available online: <https://empslocal.ex.ac.uk/people/staff/gv219/classics.d/Ekman05.pdf> (accessed on 1 March 2023).

33. Nieto, K.; Demarcq, H.; McClatchie, S. Mesoscale frontal structures in the Canary Upwelling System: New front and filament detection algorithms applied to spatial and temporal patterns. *Remote Sens. Environ.* **2012**, *123*, 339–346. [[CrossRef](#)]
34. Machu, E.; Ettahiri, O.; Kifani, S.; Benazzouz, A.; Makaoui, A.; Demarcq, H. Environmental control of the recruitment of sardines (*Sardina pilchardus*) over the western Saharan shelf between 1995 and 2002: A coupled physical/biogeochemical modelling experiment. *Fish. Oceanogr.* **2009**, *18*, 287–300. [[CrossRef](#)]

**Disclaimer/Publisher’s Note:** The statements, opinions and data contained in all publications are solely those of the individual author(s) and contributor(s) and not of MDPI and/or the editor(s). MDPI and/or the editor(s) disclaim responsibility for any injury to people or property resulting from any ideas, methods, instructions or products referred to in the content.